Supporting Information

Porphyrin Frameworks-derived N-doped Porous Carbon-confined Ru for NH₃BH₃ Methanolysis: The More Pyridinic-N, the better

Xiugang Li,[a,b] Qilu Yao,[a] Zongbao Li,[b] Hongbo Li,[a] Qi-Long Zhu,[a,c] Zhang-Hui Lu[a,*]

[a]Key Laboratory of Functional Small Molecules for Ministry of Education, College of Chemistry and Chemical Engineering, Jiangxi Normal University, Nanchang 330022, China.

[b]College of Material and Chemical Engineering, Tongren University, Tongren 554300, China.

[c]State Key Laboratory of Structural Chemistry, Fujian Institute of Research on the Structure of Matter, Chinese Academy of Sciences, Fuzhou 350002, China.

Corresponding author:

E-mail addresses: luzh@jxnu.edu.cn (Z.-H. Lu)

Table of Contents

Experimental section

References

Experimental Section

Chemicals

All chemicals from commercial sources are of reagent grade and used without further purification. Ruthenium (III) chloride ($RuCl_3$, Aladdin, >45%), methanol-D4 (CD_3OD, Aladdin, 98 atom%), sodium borohydride ($NaBH_4$, Aladdin, 98.5%), sodium borodeuteride ($NaBD_4$, Aladdin, 98 atom%), ammonium sulfate (($NH_4)_2SO_4$, Aladdin, 99%), ammonium sulfate-$^{15}N_2$ (($^{15}NH_4)_2SO_4$, Aladdin, 99 atom%), anhydrous 1,4-Dioxane ($C_4H_8O_2$, Aladdin, 99.8 atom%, $H_2O \leqslant 50$ ppm), 4,4'-biphenyldicarboxaldehyde ($C_{14}H_{10}O_2$, Aladdin, 98%), pyrrole (C_4H_5N, Aladdin, 99%), acetic acid ($C_2H_4O_2$, Aladdin, 99.5%), trifluoroacetic acid ($C_2HO_2F_3$, Aladdin, 99.5%), nitrobenzene ($C_6H_5NO_2$, Aladdin, 99%), and ammonia boron (NH_3BH_3, Aldrich, 97%) were used as received.

Characterization

Powder X-ray diffraction (XRD) patterns were carried out with X-ray diffractometer of Rigaku RINT-2200, using graphite monochromatized Cu Kα radiation ($\lambda = 1.54$ Å) at a scanning rate of 4°/min. An inductively coupled plasma (ICP) spectrophotometer (Varian, 725-ES) was used to determine the chemical components of the as-synthesized catalysts after the sample digested by microwave. Solid-state ^{13}C dipolar-decoupling Magic Angle Spinning NMR spectra were collected using a JNM-ECZ600R at 600 MHz with a rotating speed of 10 kHz and a relaxation time of 5.0 s. The ^{11}B NMR spectra were recorded using a Bruker Avance NEO 600 spectrometer (600 MHz) with a Nalorac quad probe. Organic element analysis (OEA) was carried out on an EA3000

elemental analyzer (Euro EA3000, Euro Vector, Milano, Italy). The Brunauer-Emmett-Teller (BET) equation method was used to analyze the specific surface areas, on the basis of nitrogen adsorption-desorption isotherms which was recorded on a BELSORP-mini II at 77 K. Fourier-transfer infrared spectroscopic (FT-IR) spectroscopy were carried out on a Thermo Nicolet 870 instrument with the KBr discs in the 500-4000 cm^{-1} region. X-ray photoelectron spectroscopy (XPS) analyses were carried out on an ESCALAB 250XI X-ray photoelectron spectrometer using an Al Kα source. Transmission electron microscopy (TEM), scanning transmission electron microscopy (STEM) images and energy-dispersive X-ray spectroscopy (EDS) mapping analyses were recorded on SU-8020 and JEM-2100 with Super-X EDS system under operating voltages of 300 kV. GC analysis was carried out on a FULI GC-9790II gas chromatography equipped with a TCD system and a TDX-01 chromatographic column (FULI Anal. Instrument Ltd., Wenling, China): oven temperature at 60 ℃ and detector temperature at 120 ℃.

Synthesis of BPDA-POF

BPDA-POF was synthesized via a modified solution-processed condensation polymerization [S1]. Typically, 2.10 g 4,4'-Biphenyldicarboxaldehyde (BPDA) was first solved into 100 mL acetic acid by stirring for 10 min. 1.0 mL TFA and 5.0 mL NBZ were added to the solution as the catalyst and the oxidant. After that, pyrrole (1.39 mL, 20 mmol) was added drop wise into the above solution and the colour turned into deep purple gradually. After 2 h of reaction at room temperature, the mixture was kept at 110 °C under continuous stirring for 12 h and cooled to room temperature to afford

a dark suspension. The product was filtered and washed with ethanol, dichloromethane, and ethanol to remove unreacted reagents and small porphyrin molecules. BPDA-POF was finally obtained as black powders after being dried at 60 °C for 24 h. The yield was calculated to be 96.7%.

Synthesis of Ru@PVP, Ru@POF, and Ru NPs

For comparison, Ru NPs stabilized by PVP (denoted as Ru@PVP) and BPDA-POF (denoted as Ru@POF) were synthesized using the same in-situ reduction method as for Ru@POF-NC600. The pure Ru NPs without support were also synthesized by in-situ reduction method with AB as a reductant.

Synthesis of NH_3BD_3

In a dried three-neck round bottom flask with an argon gas shield apparatus, sodium borodeuteride ($NaBD_4$, 0.02 mol) and ammonium sulfate (($NH_4)_2SO_4$, 0.02 mol), as well as anhydrous 1,4-dioxane (150 mL) were added and allowed to stir at 40 °C for 48 h until the hydrogen evolution ceases. The solvent was then removed by rotary evaporation. The crude product was dissolved in dry diethyl ether and filtered to remove any insoluble materials (repeated 3 times). The NH_3BD_3 product was obtain as small needle-like white solids after removing the solvent and vacuum drying at room temperature for 24 h (yield: 65%). The purity of the product is assessed by means of ^{11}B NMR spectroscopy (**Fig. S17**).

Synthesis of $^{15}NH_3BH_3$

$^{15}NH_3BH_3$ were synthesized using the same method as for NH_3BD_3 with $NaBH_4$ and ($^{15}NH_4)_2SO_4$ as raw materials. The purity of the product is also assessed by means of

^{11}B NMR spectroscopy (**Fig. S18**).

Caution: Hydrogen is generated during the synthesis of NH3-BD3, which is a potential fire hazard. Thus, it is recommended that the reaction should be carried out in a well-ventilated hood with an argon flow, and that the reaction vessel outlet should be led directly into the hood exhaust.

Calculation methods

The initial turnover frequency (TOF) values are calculated from the slope of the linear when the conversion reached 20%:

$$TOF = \frac{n_{H_2}}{n_{Ru} \cdot tmin} = \frac{PatmVH2/RT}{n_{Ru} \cdot tmin}$$

In the equation, n_{H2} is the mol of generated H_2 (P_{atm} is 101.325 kPa, R is 8.3145 $m^3 \cdot Pa \cdot mol^{-1} \cdot K^{-1}$, V_{H2} is the volume of generated H_2, and T is 298 K) when the conversion reached 20%, n_{Ru} is the total mole number of Ru atoms in the catalyst, and t_{min} is the time when the conversion reached 20%.

The metal dispersion (D_M) was calculated by using the equation:

$$D_M = (6n_s M)/(\rho N d_p)$$

In the equation, n_s is the number of atoms at the surface per unit area (1.63×10^{19} m^{-2} for Ru), M is the molecular weight (101.07 g mol^{-1} for Ru), ρ is the density (12.16 g·cm^{-3} for Ru), N is 6.023×10^{23} mol^{-1}, and d_p is the average particle size measured by TEM.

The corrected TOF based on the surface atoms of Ru nanoparticles was calculated by using the equation *TOF$_{corrected}$ = TOF/D$_M$*.

The dynamic influence factors of the catalytic activity, such as the dosages of AB and catalyst, as well as the reaction temperature, were calculated from the slope of the linear part of each plot when the conversion reached 50%. The activation energy (Ea) was calculated according to the equation below:
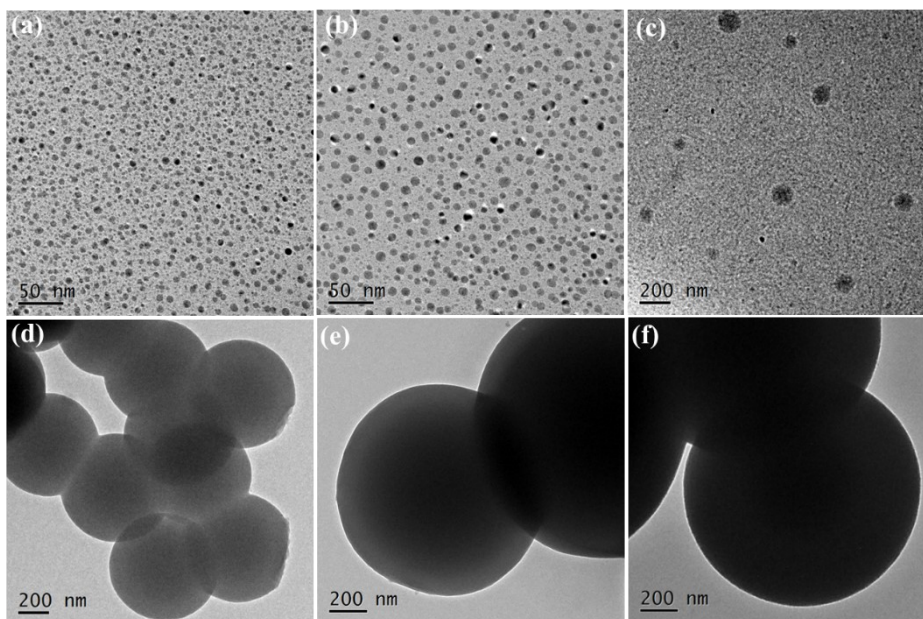
$$Ea = (lnA - lnk)RT$$

Fig. S1 TEM images of BPDA-POF; reaction was quenched after (a) 1 min, (b) 2 min,

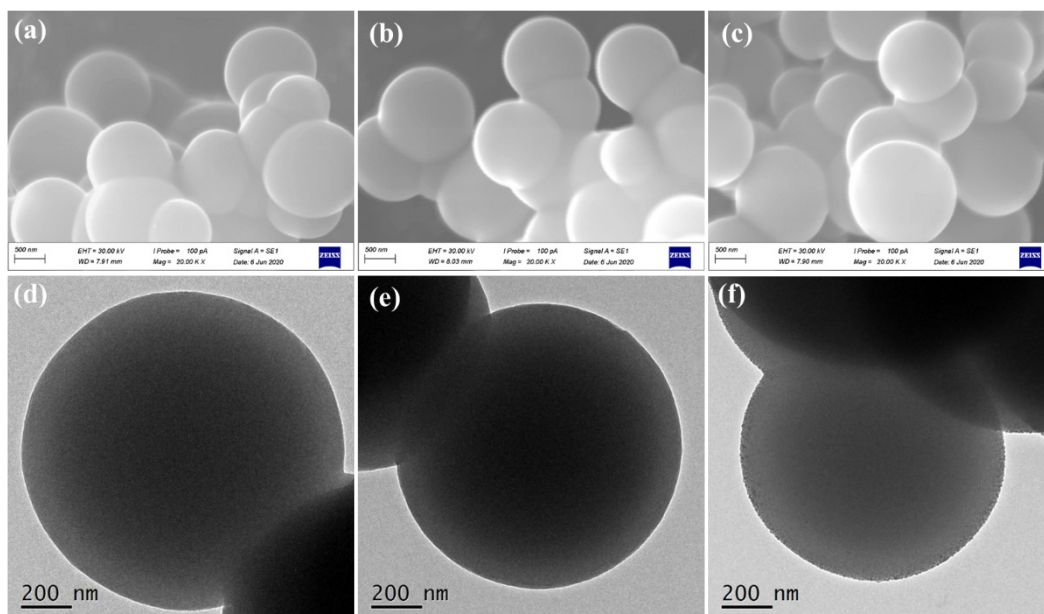(c) 5min, (d) 30 min, (e) 2 h, and (f) 12 h.

Fig. S2 Typical SEM and TEM images of (a, d) BPDA-POF, (b, e) POF-NC600, and
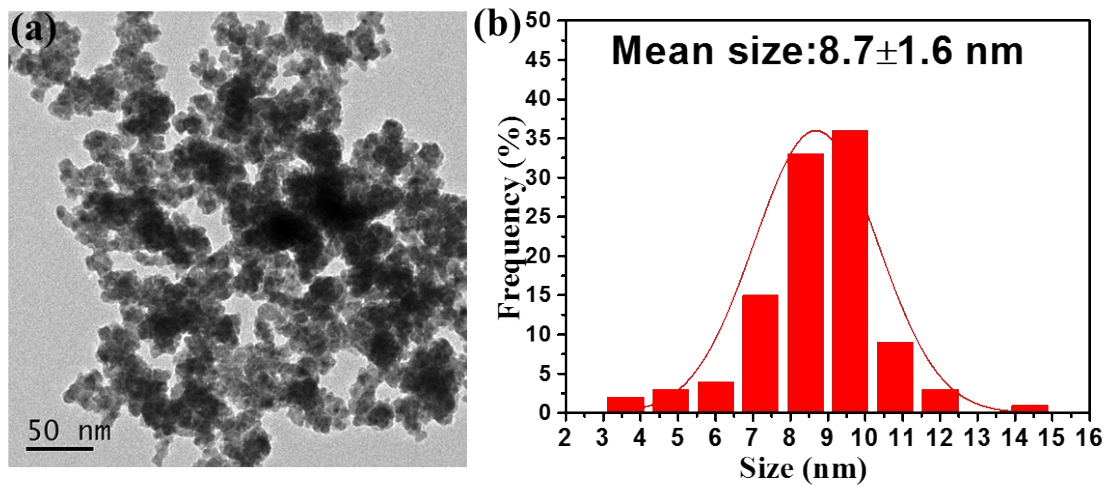
(c, f) Ru@POF-NC600.

Fig. S3 Representative TEM image and the corresponding distribution size histograms of Ru NPs without support.
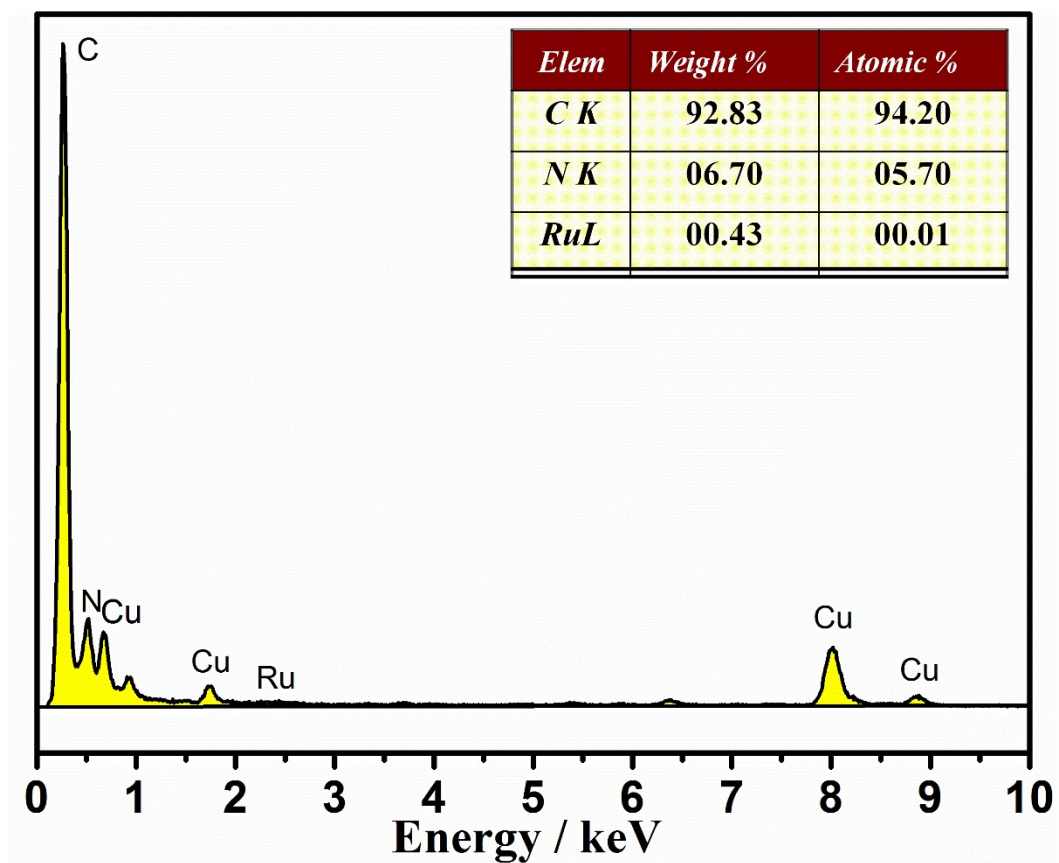
Elem	Weight %	Atomic %
C K	92.83	94.20
N K	06.70	05.70
RuL	00.43	00.01

Fig. S4 The corresponding EDX spectrum of Ru@POF-NC600 catalyst. The Cu signal originates from Cu grid.
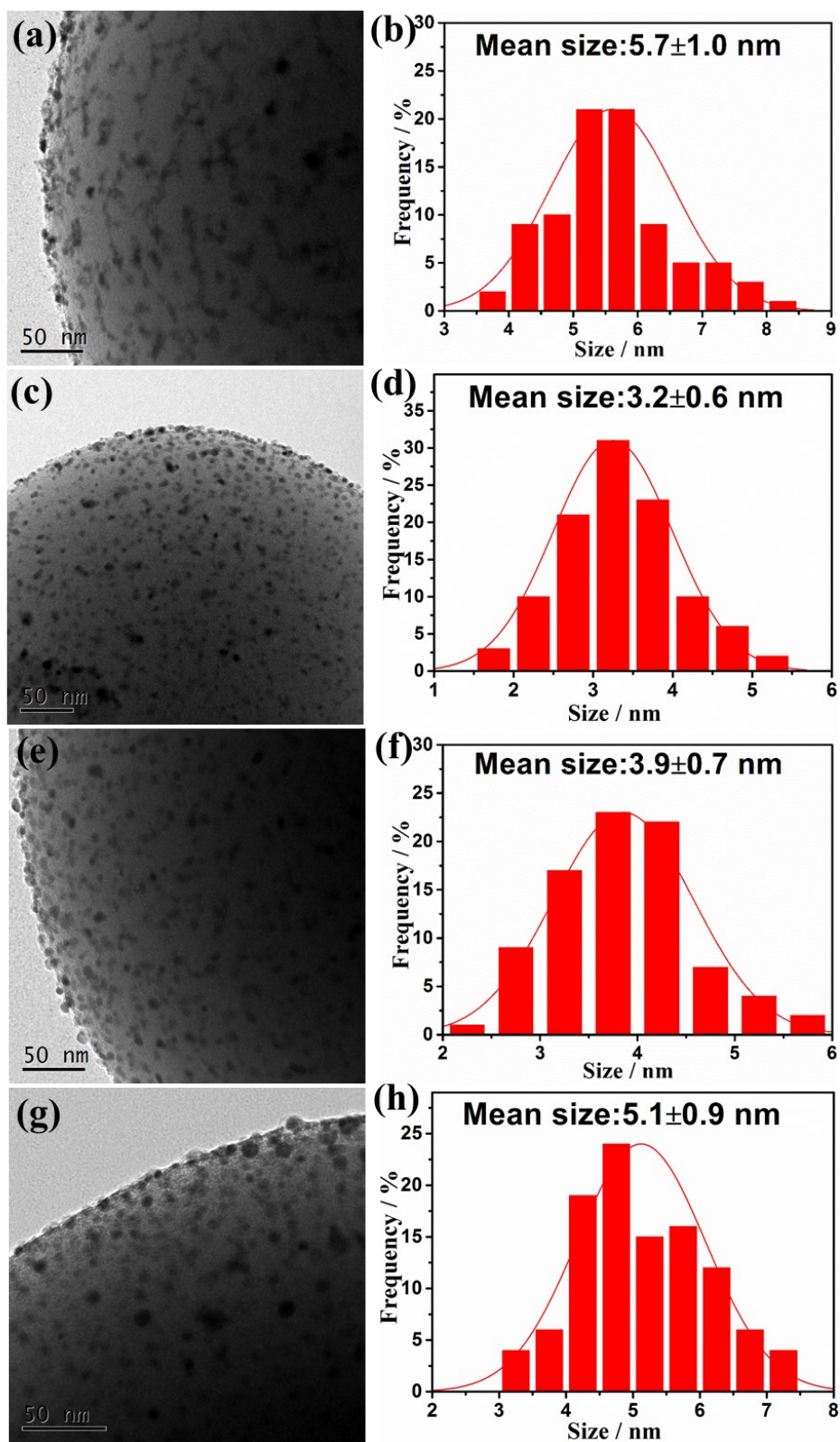
Fig. S5 Representative TEM images and the corresponding distribution size histograms of (a, b) Ru@POF-NC500, (c, d) Ru@POF-NC600, (e, f) Ru@POF-NC700, and (g, h) Ru@POF-NC800.
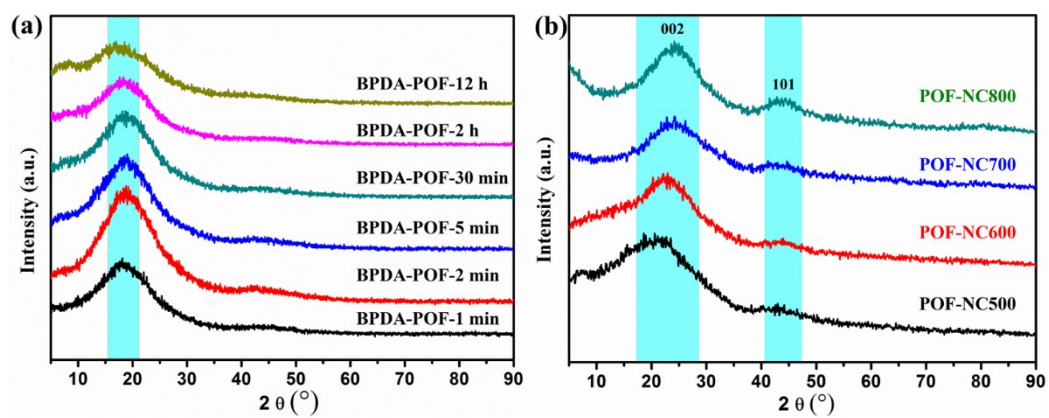
Fig. S6 XRD patterns of (a) BPDA-POF quenched after different reaction times; (b) POF-NCT with different pyrolysis temperatures.
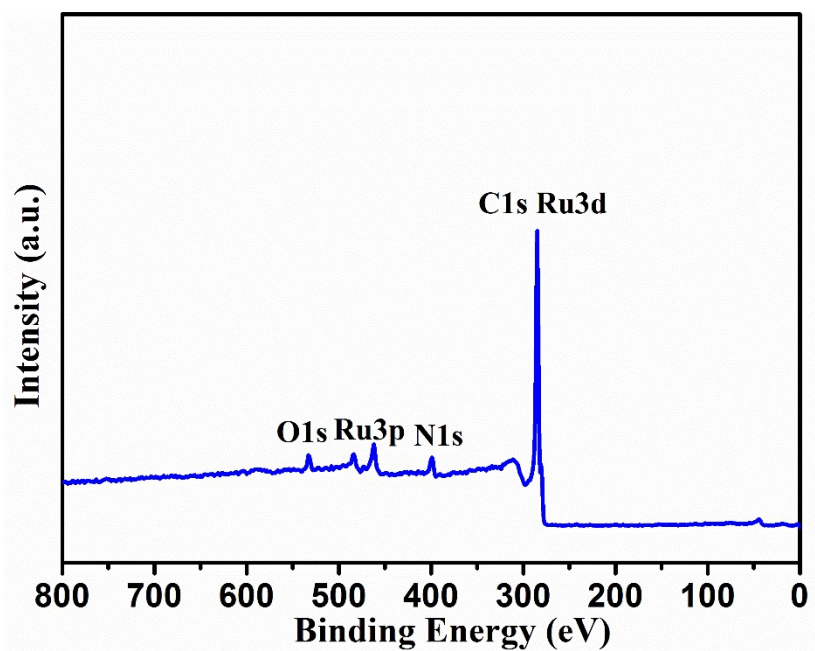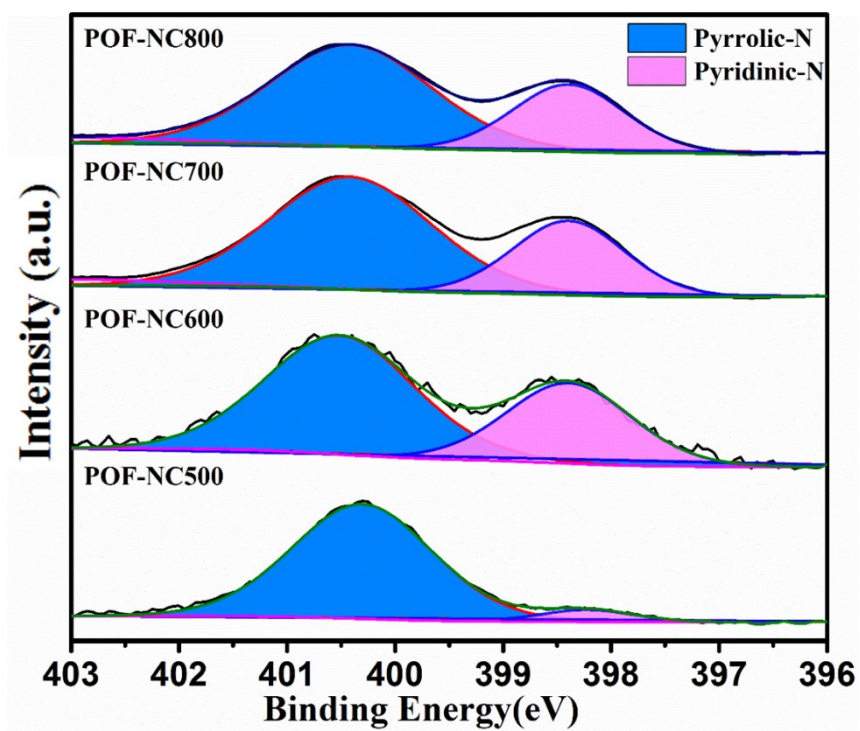
Fig. S7 XPS survey data of Ru@POF-NC600.

Fig. S8 High-resolution N 1s XPS spectra of POF-NCT prepared at different pyrolysis temperatures.
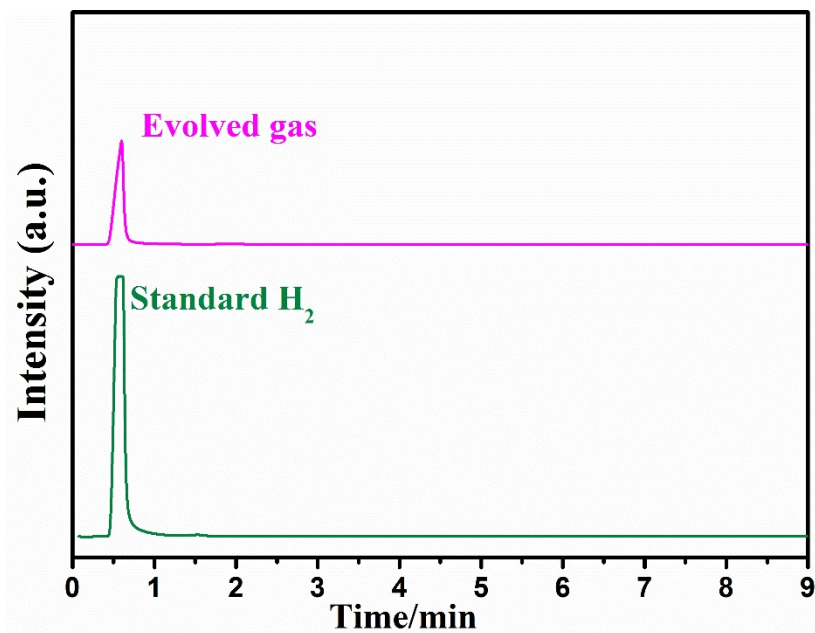
Fig. S9 GC spectra for evolved gas from AB methanolysis.
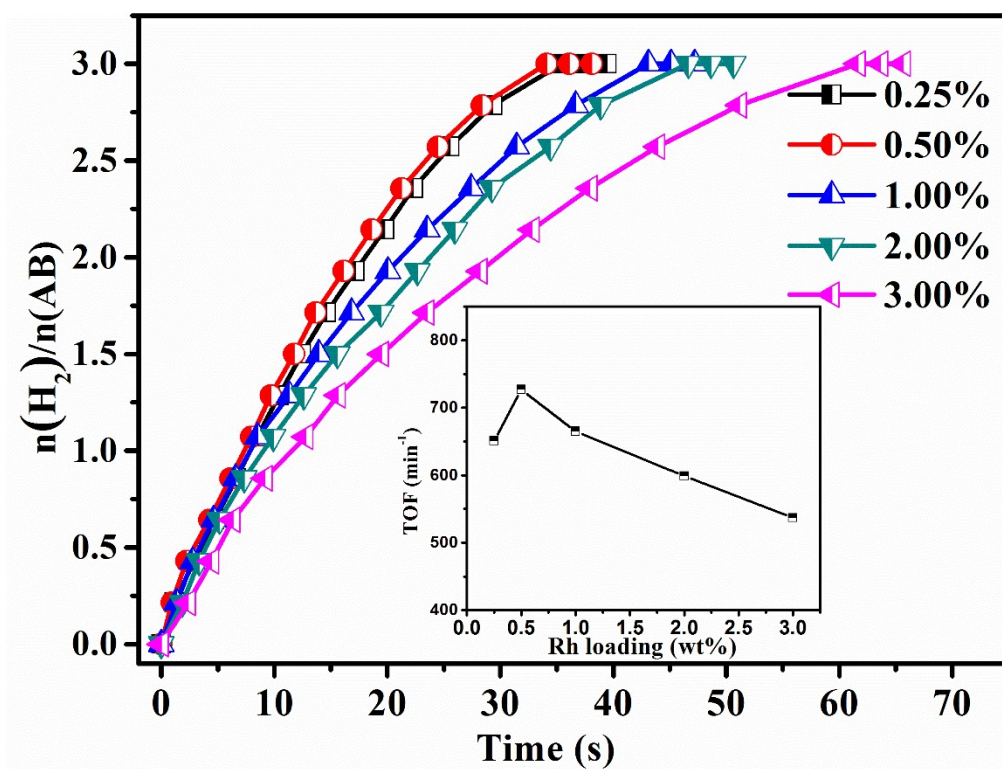
Fig. S10 Time course plots of H_2 generation for methanolysis of AB over Ru@POF-NC600 with different loadings of Ru at 298 K; the insert is the corresponding initial TOF values.
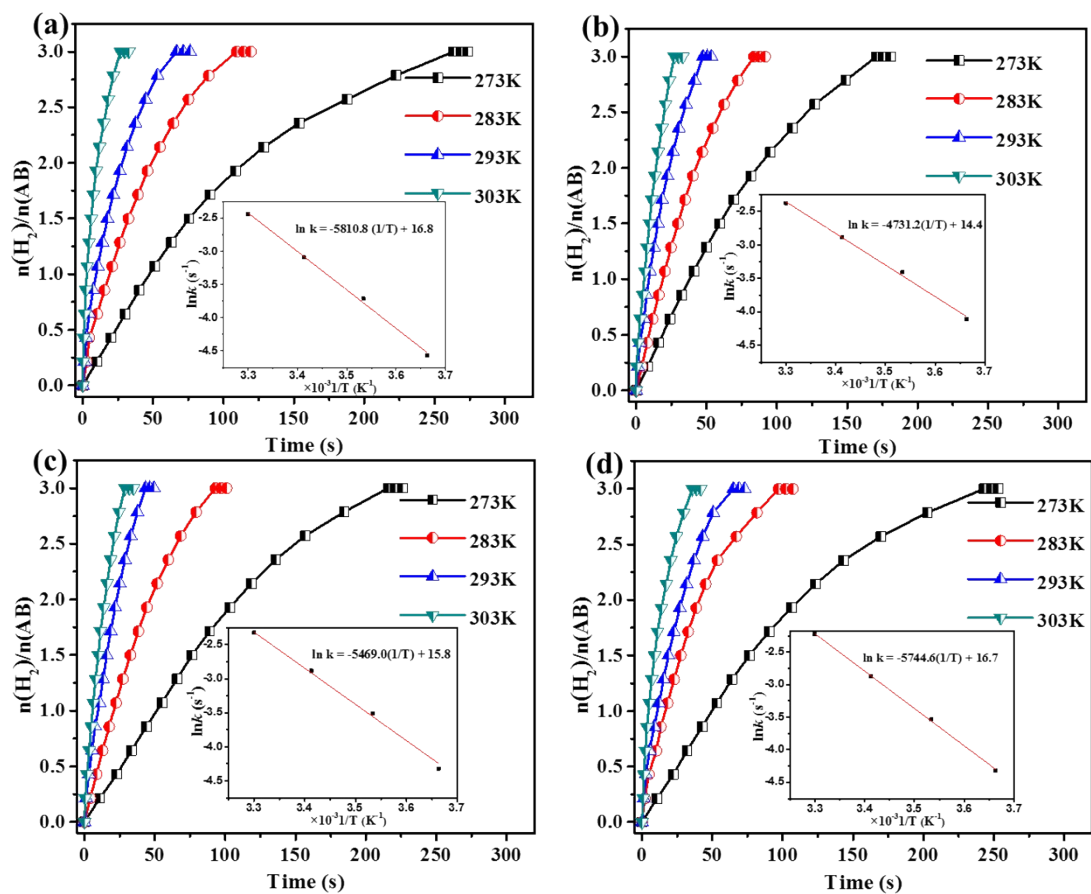
Fig. S11 Time course plots of H$_2$ generation for AB methanolysis over (a) Ru@POF-NC500, (b) Ru@POF-NC600, (c) Ru@POF-NC700, and (d) Ru@POF-NC800 with different reaction temperatures. The insert is the corresponding Arrhenius plots.
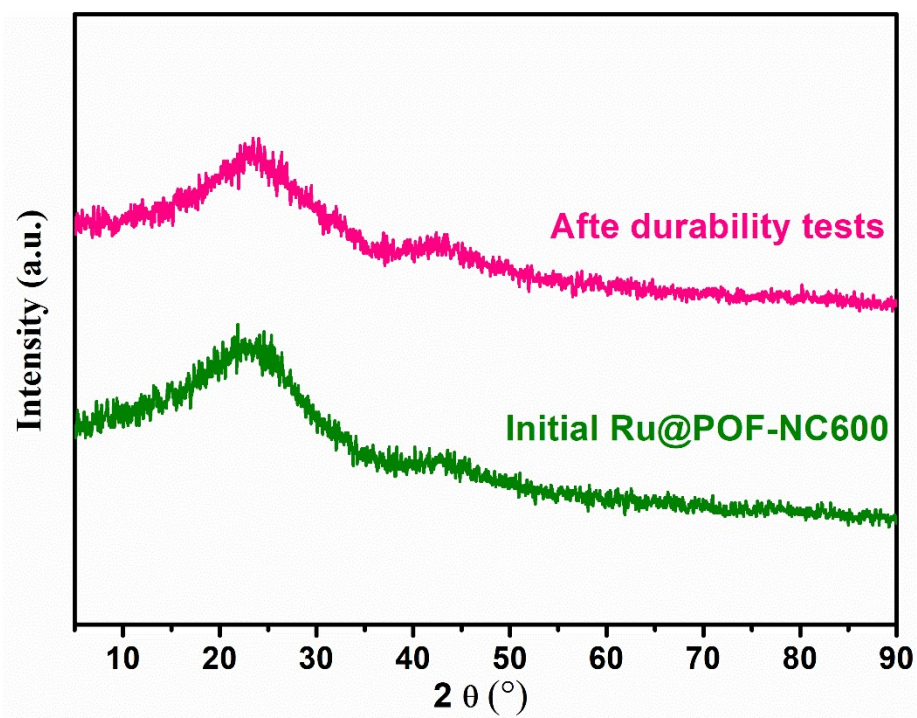
Fig. S12 Powder XRD patterns of the as-synthesized Ru@POF-NC600 catalyst before and after durability tests.
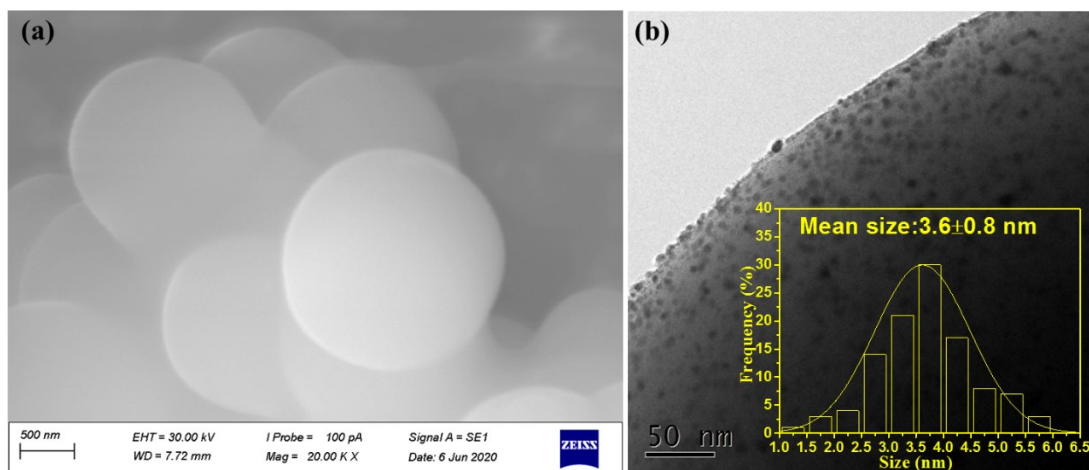
Fig. S13 Typical (a) SEM and (b) TEM images of Ru@POF-NC600 after five runs.

The inset of (b) is the corresponding particle size distribution histogram of Ru NPs.
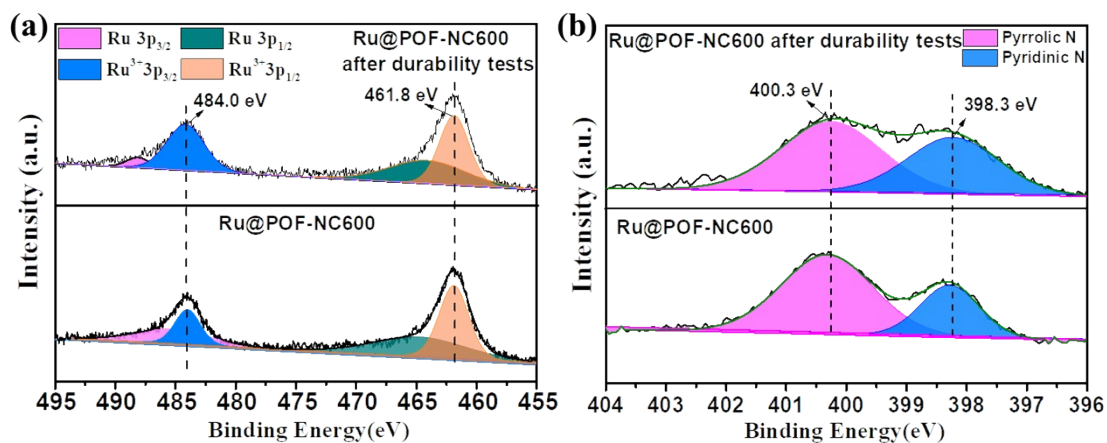
Fig. S14 Ru 3p and N 1s XPS of fresh Ru@POF-NC600 and Ru@POF-NC600 after

durability tests.
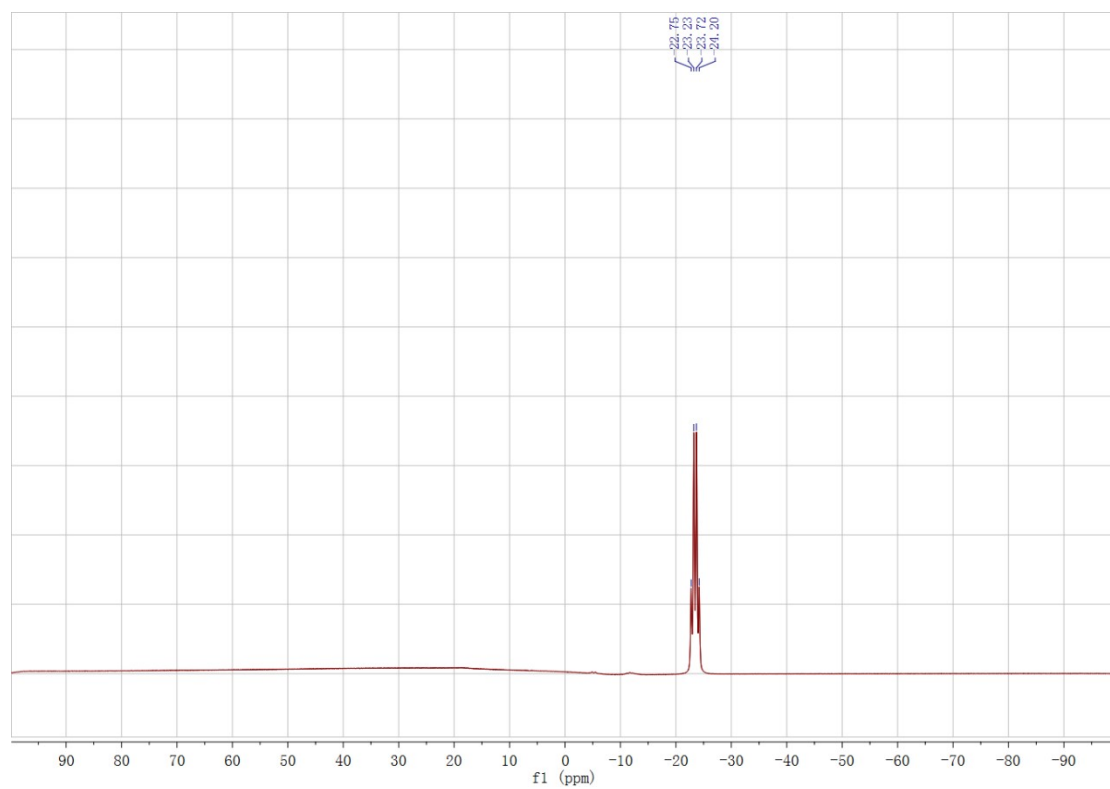
Fig. S15 ^{11}B NMR spectrum of the system before NH_3BH_3 methanolysis in CD_3OD.
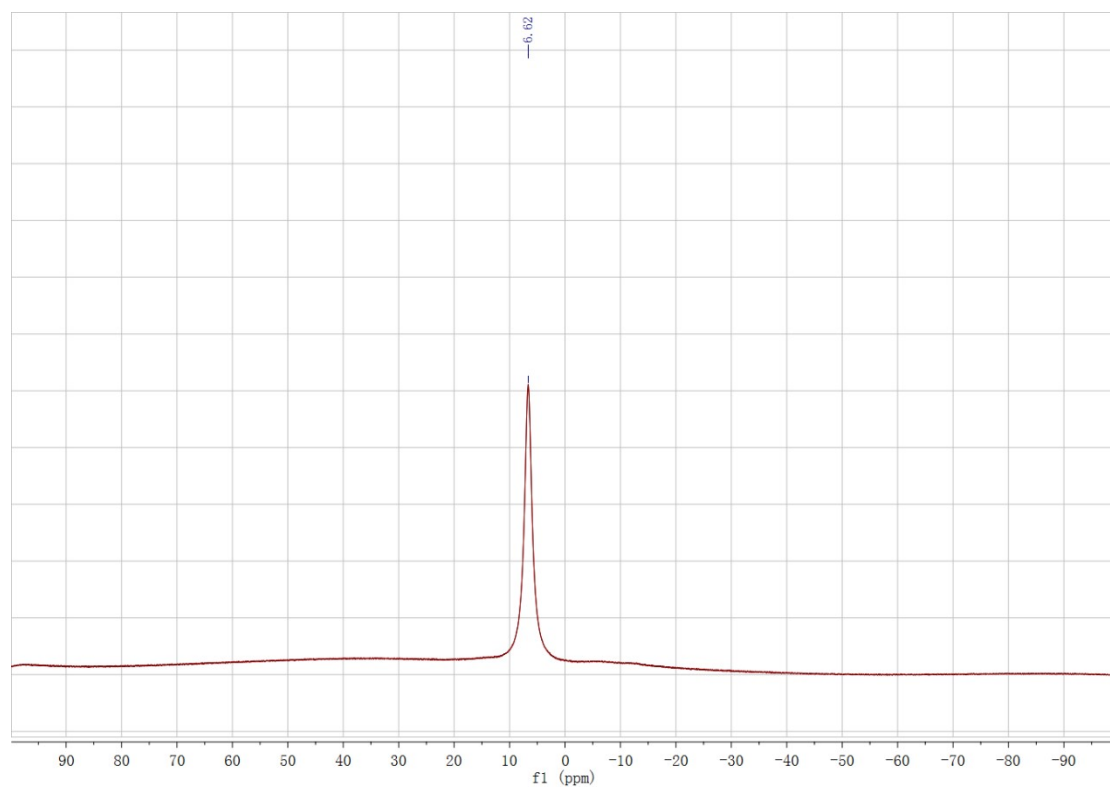
Fig. S16 ^{11}B NMR spectrum of the system after NH_3BH_3 methanolysis in CD_3OD.
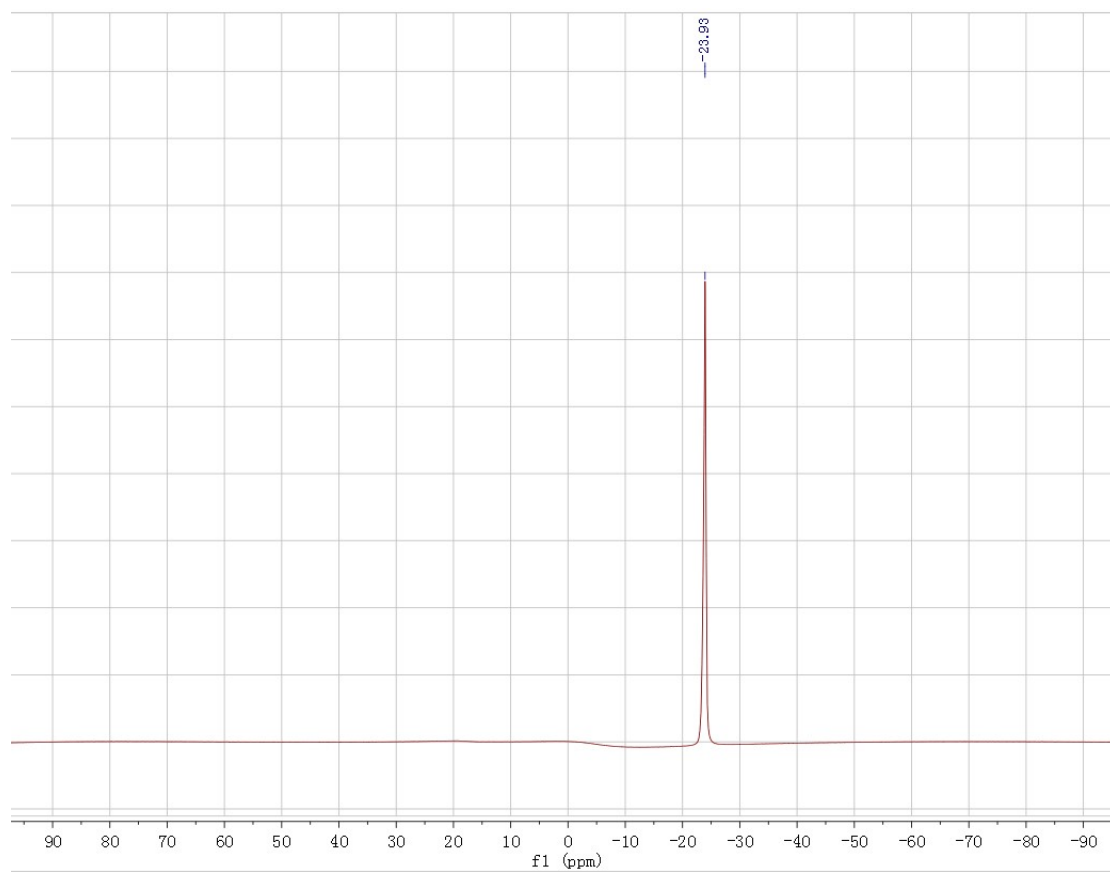
Fig. S17 ^{11}B NMR spectrum of NH_3BD_3 (in CD_3OD).
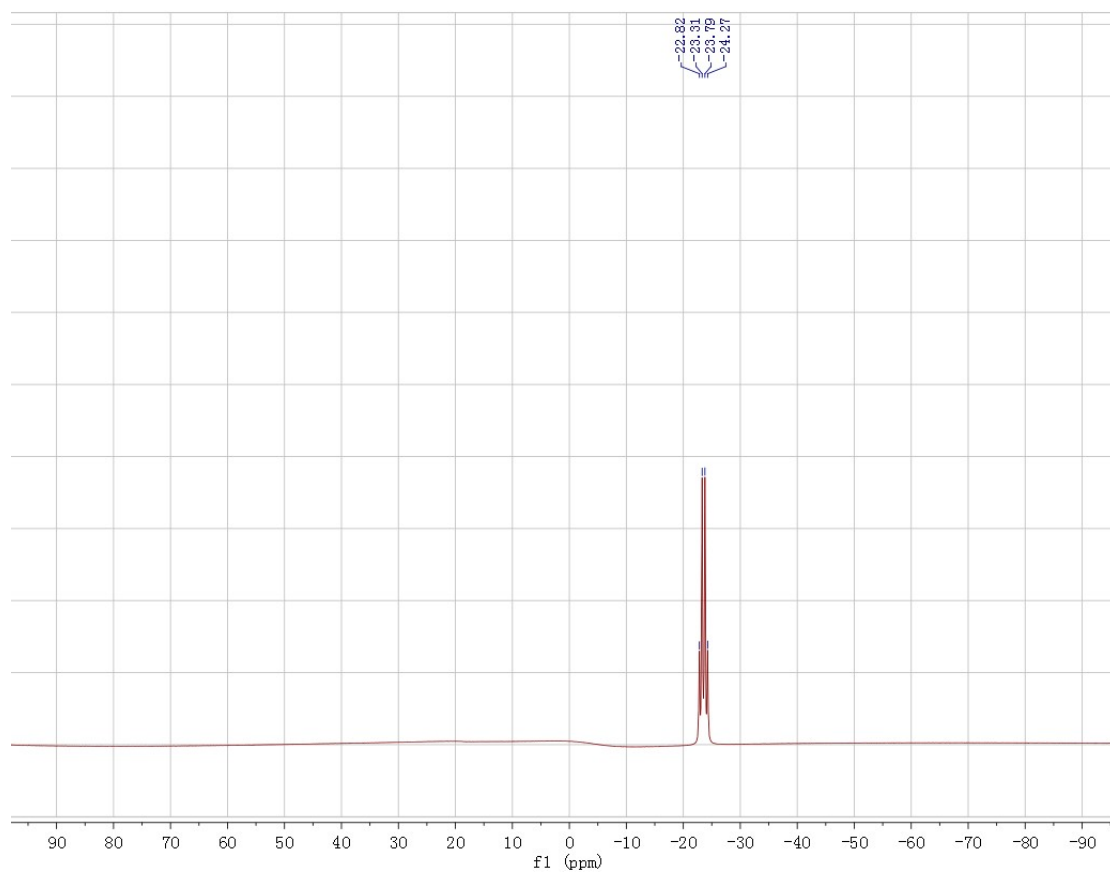
Fig. S18 ^{11}B NMR spectrum of ^{15}NH$_3$BH$_3$ (in CD$_3$OD).

Tab. S1 The particle size and metal dispersion (D_M) of Ru@POF-NCT prepared at different pyrolysis temperatures.

Samples	Particle size (nm)	D_M (%)
Ru@POF-NC500	5.7	23.7
Ru@POF-NC600	3.2	42.2
Ru@POF-NC700	3.9	34.6
Ru@POF-NC800	5.1	26.5

Tab. S2 Texture parameters of POF-NCT with different pyrolysis temperatures.

Samples	C(%)*	N(%)*	Pyrrolic-N(%)#	Pyridinic-N(%)#
POF-NC500	90.22	7.93	7.26	0.67
POF-NC600	90.88	6.39	4.02	2.37
POF-NC700	92.07	5.29	3.47	1.82
POF-NC800	93.27	4.28	2.89	1.39

* The contents of C and N are based on OEA tests.

 # The contents of pyrrolic-N and pyridinic-N are based on XPS of N1s and OEA tests.

Tab. S3 Catalytic activities of different catalysts for methanolysis of AB.

Catalyst	Temp. (K)	TOF (min^{-1})	E_a(kJ/mol)	Ref.
Ru@POF-NC600	298	727[a] (423[b])	39.4	This Work
Rh-PRO/C	298	411[b]	38.2	S2
AgPd alloy	298	366.4[b]	37.5	S3
Ru@PCC-2	298	304[b]	--	S4
HPRhS	298	292[b]	--	S5
Rh/nanoAl$_2$O$_3$	298	218[a]	48	S6
Rh/CC3-R-homo	298	215[b]	--	S7
Pd@RCC3	298	176[b]	--	S8
Rh/nanoSiO$_2$	298	168[a]	62	S9
Rh/nanoHAP	298	147[a]	56	S10
Rh/nanoCeO$_2$	298	144[a]	64.6	S11
Ru/MMT	298	118[b]	23.8	S12
Pd/GNS	298	101[b]	46	S13
Ru/graphene	298	99.4[a]	54.1	S14
PVP-stabilized Ru	298	67[b]	58	S15
Cu$_{48}$Pd$_{52}$ alloy/C	298	53.2[b]	--	S16
Cu$_{36}$Ni$_{64}$/Graphene	298	49.1[b]	24.4	S17
Co$_{48}$Pd$_{52}$/C	298	27.7[b]	25.5	S18
Cu@Cu$_2$O@CuO/ C	298	24[b]	67.9	S19
PVP-stabilized Pd	298	22.3[b]	35	S20
PVP-stabilized Ni	298	12.1[b]	62	S21
Co-Ni-B	298	10[b]	--	S22

[a]The initial TOF values are calculated from the slope of the linear when the conversion reached 20%.
[b]The total TOF values are calculated based on 100% conversion of H$_2$.

Tab. S4 The particle size, initial TOF values, and corrected TOF values (TOF$_{corrected}$) of Ru@POF-NCT prepared at different pyrolysis temperatures.

Samples	Particle size (nm)	Initial TOF (min^{-1})	Corrected TOF (min^{-1})*
Ru@POF-NC500	5.7	391	1650
Ru@POF-NC600	3.2	727	1723
Ru@POF-NC700	3.9	585	1682
Ru@POF-NC800	5.1	442	1668

*The corrected TOF values based on the surface atoms of Ru NPs are calculated by using the equation $TOF_{corrected} = TOF/D_M$**.**

References

(S1) B.-Q. Li, S.-Y. Zhang, X. Chen, C.-Y. Chen, Z.J. Xia, Q. Zhang, One-Pot Synthesis of Framework Porphyrin Materials and Their Applications in Bifunctional Oxygen Electrocatalysis, Adv. Funct. Mater. 29 (2019) 1901301.

(S2) W. Luo, W. Cheng, M. Hu, Q. Wang, X. Cheng, Y. Zhang, Y. Wang, D. Gao, J. Bi, G. Fan, Ultrahigh Catalytic Activity of L-Proline-Functionalized Rh Nanoparticles for Methanolysis of Ammonia Borane, ChemSusChem 12 (2018) 535-541.

(S3) D. Sun, P. Li, B. Yang, Y. Xu, J. Huang, Q. Li, Monodisperse AgPd alloy nanoparticles as a highly active catalyst towards the methanolysis of ammonia borane for hydrogen generation, RSC Adv. 6 (2016) 105940-105947.

(S4) Y. Fang, J. Li, T. Togo, F. Jin, Z. Xiao, L. Liu, H. Drake, X. Lian, H. Zhou, Ultra-small face-centered-cubic Ru nanoparticles confined within a porous coordination cage for dehydrogenation, Chem 4 (2018) 555-563.

(S5) H. Zou, B. Jin, R. Wang, Y. Wu, H. Yang, S. Qiu, Iodide-mediated templating synthesis of highly porous rhodium nanospheres for enhanced dehydrogenation of ammonia borane, J. Mater. Chem. A 6 (2018) 24166-24174.

(S6) D. Özhava, S. Özkar, Nanoalumina-supported rhodium (0) nanoparticles as catalyst in hydrogen generation from the methanolysis of ammonia borane, Mol. Catal. 439 (2017) 50-59.

(S7) J.-K. Sun, W.-W. Zhan, T. Akita, Q. Xu, Toward Homogenization of Heterogeneous Metal Nanoparticle Catalysts with Enhanced Catalytic Performance: Soluble Porous Organic Cage as a Stabilizer and Homogenizer, J. Am. Chem. Soc. 137 (2015) 7063-7066.

(S8) X. Yang, J.-K. Sun, M. Kitta, H. Pang, Q. Xu, Encapsulating highly catalytically active metal nanoclusters inside porous organic cages, Nat. Catal. 1 (2018) 214.

(S9) D. Özhava, S. Özkar, Rhodium (0) nanoparticles supported on nanosilica: highly active and long lived catalyst in hydrogen generation from the methanolysis of ammonia borane, Appl. Catal. B-Environ. 181 (2016) 716-726.

(S10) D. Özhava, S. Özkar, Rhodium(0) nanoparticles supported on hydroxyapatite nanospheres and further stabilized by dihydrogen phosphate ion: A highly active catalyst in hydrogen generation from the methanolysis of ammonia borane, Int. J. Hydrogen. Energy 40 (2015) 10491-10501.

(S11) D. Özhava, S. Özkar, Nanoceria supported rhodium (0) nanoparticles as catalyst for hydrogen generation from methanolysis of ammonia borane, Appl. Catal. B-Environ. 237 (2018) 1012-1020.

(S12) H. Dai, X. Kang, P. Wang, Ruthenium nanoparticles immobilized in montmorillonite used as catalyst for methanolysis of ammonia borane, Int. J. Hydrogen Energy 35 (2010) 10317-10323.

(S13) Y. Karataş, M. Gülcan, M. Çelebi, M. Zahmakiran, Pd (0) nanoparticles decorated on graphene nanosheets (GNS): synthesis, definition and testing of the catalytic performance in the methanolysis of ammonia borane at room conditions, ChemistrySelect 2 (2017) 9628-9635.

(S14) S. Peng, J. Liu, J. Zhang, F. Wang, An improved preparation of graphene supported ultrafine ruthenium (0) NPs: Very active and durable catalysts for H_2 generation from methanolysis of ammonia borane, Int. J. Hydrogen Energy 40 (2015) 10856-10866.

(S15) H. Erdoğan, Ö. Metin, S. Özkar, Hydrogen generation from the methanolysis of ammonia borane catalyzed by in situ generated, polymer stabilized ruthenium (0) nanoclusters, Catal. Today 170 (2011) 93-98.

(S16) P. Li, Z. Xiao, Z. Liu, J. Huang, Q. Li, D. Sun, Highly efficient hydrogen generation from methanolysis of ammonia borane on CuPd alloy nanoparticles, Nanotechnology 26 (2014) 25401.

(S17) C. Yu, J. Fu, M. Muzzio, T. Shen, D. Su, J. Zhu, S. Sun, CuNi nanoparticles assembled on graphene for catalytic methanolysis of ammonia borane and hydrogenation of nitro/nitrile compounds, Chem. Mater. 29 (2017) 1413-1418.

(S18) D. Sun, V. Mazumder, O. Metin, S. Sun, Methanolysis of ammonia borane by CoPd nanoparticles, ACS Catal. 2 (2012) 1290-1295.

(S19) S.B. Kalidindi, U. Sanyal, B.R. Jagirdar, Nanostructured Cu and Cu@Cu_2O core shell catalysts for hydrogen generation from ammonia-borane, Phys. Chem. Chem. Phys. 10 (2008) 5870-5874.

(S20) H. Erdoğan, Ö. Metin, S. Özkar, In situ-generated PVP-stabilized palladium (0) nanocluster catalyst in hydrogen generation from the methanolysis of ammonia-borane, Phys. Chem. Chem. Phys. 11 (2009) 10519-10525.

(S21) D. Özhava, N.Z. Kılıçaslan, S. Özkar, PVP-stabilized nickel (0) nanoparticles as catalyst in hydrogen generation from the methanolysis of hydrazine borane or ammonia borane, Appl. Catal. B-Environ. 162 (2015) 573-582.

(S22) S.B. Kalidindi, A.A. Vernekar, B.R. Jagirdar, Co-Co_2B, Ni-Ni_3B and Co-Ni-B nanocomposites catalyzed ammonia-borane methanolysis for hydrogen generation, Phys. Chem. Chem. Phys. 11 (2009) 770-775.